Accepted Manuscript
Version of record at: https://doi.org/10.1002/nbm.4616

Quantitative Effects of Off-Resonance Related Distortion on Brain Mechanical Property Estimation with Magnetic Resonance Elastography

Grace McIlvain[1], Matthew D J McGarry[2], Curtis L Johnson[1]

1 Department of Biomedical Engineering, University of Delaware; Newark, DE

2 Thayer School of Engineering, Dartmouth College, Hanover, NH

Corresponding Author:
Curtis L Johnson, PhD
150 Academy St
Newark, DE 19716
clj@udel.edu

Approximate Word Count: 7000

ABSTRACT

Off-resonance related geometric distortion can impact quantitative MRI techniques, such as magnetic resonance elastography (MRE), and result in errors to these otherwise sensitive metrics of brain health. MRE is a phase contrast technique to determine mechanical properties of tissue by imaging shear wave displacements and estimating tissue stiffness through inverse solution of Navier's equation. In this study, we systematically examined the quantitative effects of distortion and corresponding correction approaches on MRE measurements through a series of simulations, phantom models, and *in vivo* brain experiments. We studied two different *k*-space trajectories, echo-planar imaging and spiral, and we determined that readout time, off-resonance gradient strength, and the combination of readout direction and off-resonance gradient direction impact estimated mechanical properties. Images were also processed through traditional distortion correction pipelines, and we found that the correction mechanisms each work well for reducing stiffness errors but are limited in cases of very large distortion. The ability of MRE to detect subtle changes to neural tissue health relies on accurate, artifact-free imaging, and thus off-resonance related geometric distortion must be considered when designing sequences and protocols by limiting readout time and applying correction where appropriate.

KEY WORDS: viscoelasticity, brain, distortion, magnetic resonance elastography, off-resonance

Accepted Manuscript
Version of record at: https://doi.org/10.1002/nbm.4616

Abbreviations

MRE Magnetic Resonance Elastography
MRI Magnetic Resonance Imaging
EPI Echo Planar Imaging
GRAPPA GeneRalized Autocalibrating Partial Parallel Acquisition
SENSE SENSitivity Encoding
FSL FMRIB Software Library
FUGUE FSL's Utility for Geometrically Unwarping EPIs
NLI Nonlinear Inversion
LDI Local Direct Inversion
FLIRT FSL's Linear Image Registration Tool
AP Anterior to Posterior
PA Posterior to Anterior
NUFFT Nonuniform Fast Fourier Transform
RF Radio Frequency
FOV Field-of-View
FFT Fast Fourier Transform
TE Echo Time
TR Repetition Time
MNI Montreal Neurologic Institute
MPRAGE Magnetization Prepared Rapid Acquisition Gradient Echo

1. INTRODUCTION

Magnetic resonance elastography (MRE) is a phase contrast-based MRI technology that can create whole-brain mechanical property maps *in vivo* through mechanical vibration[1]. These mechanical properties have been related to development[2,3], aging[4–6], and neurodegenerative disease[7–9], and show promise towards clinically assessing neural tissue health[10–13]. The MRE field has made substantial advances in data acquisition to improve resolution and imaging speed, however, these improvements are often limited by signal-to-noise ratio and artifacts including off-resonance related geometric distortion. Distortion manifests as an inaccurate representation of the imaged object due to bending, warping, shifting, or overlapping pixels[14] and is exacerbated by extended readout times[15,16], which can be particularly long when developing high-resolution protocols[17]. MRE works by propagating shear waves through the brain at a specific frequency and using motion encoding gradients to encode their displacement and propagation into the phase of the MRI signal[18]. Regional tissue stiffness is detected by its effect on wave propagation; therefore, distortion of the image, and thus the imaged wavefield, will result in inaccurate mechanical property measurements.

Sequence design is a critical factor in minimizing image distortion in MRE. High-resolution protocols are desirable for improving accuracy of MRE, however, these protocols often require long readout times, leading to increased distortion[19]. Echo-planar imaging (EPI) scans are kept short by capturing the entire k_{xy}-plane in one shot, but require long readout times, therefore achievable resolution is limited. Parameters to consider in high-resolution EPI sequence development are bandwidth and parallel imaging techniques, such as GRAPPA[20] or SENSE[21], which shorten readout time by undersampling k_y lines, as well as interleaving EPI shots to shorten single shot readout time. In spiral MRE, interleaved shots are nearly always used to reduce readout time[22] as the use of interleaved trajectories allows for data to be collected at higher resolution[19,23], though additional trajectories increase the total scan time proportional to the number of trajectories. In the case of spiral imaging, all of the high frequency data is sampled at the end of the data readout, therefore the effects of distortion can appear as spatial blurring[24,25]. Finding the critical readout time per shot that leads to minimal distortion, and thus minimal error in estimated properties, but that also maintains acceptable scan time, is necessary in the development of high-resolution MRE.

Minimizing error through short readout times is not always possible, and regions of magnetic field inhomogeneity are always present in the brain, therefore techniques for correction of off-resonance related distortion can be used. Distortion correction approaches exist for MRI images with different readouts and contrasts[16], however, these methods are not widely used in MRE and it is not known how well they perform in recovering the correct three-dimensional MRE wavefields for mechanical property estimation. Correction tools that have previously been used in EPI include FUGUE, which utilizes a separately collected map of the magnetic field[26] to retrospectively correct mis-mapped pixels, and TOPUP, which requires collection of images with opposing polarity phase-encoding directions and thus distortion in opposite directions[27]. TOPUP mathematically maximizes similarities between the opposing images to create a fieldmap that is then used to correct distortion. Distortion in spiral images can be addressed during iterative image reconstruction by including off-resonance effects from a fieldmap in the signal model through time-segmentation techniques[28]. Each of these correction mechanisms have been shown to adequately correct cases of minimal distortion, but they are increasingly inaccurate with more distortion and have an upper limit on correction accuracy[29–31].

In this study, we aim to quantitatively assess the impact of geometric distortion on MRE property estimates. While avoiding excessive distortion has been recognized as important in the MRE literature[23], and correction for off-resonance effects in spiral[19] and EPI[32] sequences has been used previously, these effects have only been qualitatively considered without establishing quantitative guidelines for sequence design and image reconstruction. Here we use simulated fieldmaps and *k*-space trajectories to understand the quantitative effects of distortion in MRE and we validate our findings in phantoms and *in vivo*. We aim to identify functional limits of distortion influence in MRE and to understand how data readout times affect that level of distortion. We also examine traditional MRI distortion correction mechanisms to validate and benchmark their performance in MRE.

2. METHODS

We used 1) simulations, 2) phantoms, and 3) *in vivo* brains in this study to examine the effects of distortion on MRE mechanical property calculations, with aspects of each experiment described below. To examine the impact of distortion on estimated stiffness maps, all displacement fields were processed using the finite element-based nonlinear inversion algorithm (NLI)[33] and an algebraic local direct inversion (LDI)[34]. These inversions create spatial maps of the complex-valued viscoelastic shear modulus, $G^* = G' + iG''$, where G' and G'' are the storage and loss modulus, respectively. LDI algebraically solves the Navier's equation under a series of assumptions including local spatial homogeneity of material properties that results in 3rd order spatial derivatives. Here we use an LDI approach incorporating the following parameters: smoothing of displacement fields with a Gaussian kernel (10 mm kernel with 2 mm standard deviation), curl filtering to remove longitudinal waves (6 mm kernel size), a Laplacian operator calculated with 14 mm kernel size, and combination of wave fields using total least squares[34]. NLI works by fitting a heterogenous finite element mechanical model to the MRE displacement data and iteratively solving for a shear modulus distribution that minimizes the difference between measured and calculated displacements. From the shear modulus we calculate shear stiffness as $\mu = 2|G^*|^2/(G' + |G^*|)$[35], which is the parameter commonly reported in brain MRE literature[7,36,37]. Octahedral-shear-strain signal-to-noise ratio (OSS-SNR)[38] was calculated for each phantom and *in vivo* brain image, and is a measure of SNR commonly used in MRE, where OSS-SNR > 3 is sufficient for stable inversions and reliable property maps.

2.1 Simulation Experiments

Simulation experiments were performed to examine effect of a range of field inhomogeneities and different sampling trajectories on estimated stiffness. The simulation procedure is illustrated in Figure S2, and included generating a realistic, distortion-free displacement dataset that was then encoded using both EPI and spiral trajectories with different patterns of field inhomogeneity, and then reconstructed and inverted.

A realistic MRE displacement dataset was simulated using high-resolution MRE data from a single subject[39] with 1.25 mm isotropic resolution with a 192x192 matrix size and field-of-view of 240 x 240 mm^2 to capture as much geometric detail as possible given imaging SNR constraints and memory limitations for the finite element solver; the 1.25 mm resolution of this data results in near mesh convergence[40]. Using the subject anatomy, mechanical properties of gray matter, white matter, and subcortical gray matter structures were assigned values derived from literature. The complex-valued shear modulus, G*, was assigned to the simulation as $G^* = 2.11 + 0.86i$ kPa for gray matter and $G^* = 2.53 + 1.14i$ kPa for white matter, with subcortical structures having assigned values as reported by Johnson et al[41]. A finite element solution of the governing equations for steady-state vibration of a viscoelastic material was used to compute whole-brain displacement data for this geometry and distribution of properties. Displacement boundary conditions were assigned from the measured MRE displacements on the exterior brain surface to produce realistic simulated displacement fields[42,43].

The output of the simulation is a set of complex-valued displacement amplitude fields at 1.25 mm resolution. From these simulated displacements, we created a set of complex objects representing a typical MRE dataset with displacement from four phase offsets in each of the three cardinal directions encoded in the phase of the object, and with a common magnitude from the original input image. These objects were encoded in *k*-space using a direct Fourier transform with different prescribed EPI and spiral trajectories, as described below. Each trajectory was designed for a 120 x 120 matrix and thus 2.0 mm resolution on the 240 x 240 mm^2 FOV, and resulting images were reconstructed at that resolution to avoid the less realistic case arising from identical forward and inverse problem meshes during model-based inversions such as NLI. Prior to 2D *k*-space sampling, the object was downsampled in the slice direction to a 2.0 mm slice thickness, and the final images comprised 30 axial slices. Images were reconstructed from simulated *k*-space using an iterative algorithm that incorporates the nonuniform fast Fourier transform (NUFFT)[44].

Simulated objects also had field inhomogeneity gradients added to induce distortion in the reconstructed images. Two field-inhomogeneity gradient patterns were used: 1) Linearly increasing gradients, which were applied across the entire simulated object and used to understand mechanical property errors under specific distortion thresholds, such as would occur across a localized brain region, and 2) "realistic" fieldmaps with gradients that would resemble the inhomogeneity seen at the interface of the sinus cavity[45]. The linear field gradients uniformly increased in either the positive or negative direction, with a gradient that was varied per simulation. The maximum values of the field inhomogeneities increased in increments of +/- 8 Hz/cm, from 0 Hz/cm (uniform) as the least distorted case, and -64 to 64 Hz/cm as the most distorted case, for a total of 8 linear fieldmap conditions. Linear gradient experiments were conducted with fieldmap gradients applied separately along each of the three primary orthogonal directions (i.e. phase encode, readout, and slice select). The realistic fieldmaps were created with three inhomogeneities in the approximate locations of the sinus cavity and the ear canals simulated as 3D Gaussian functions. The Gaussian function for the sinus cavity inhomogeneity was assigned to have a width of 16 pixels, and the two ear-canal inhomogeneities were assigned to have a width of 8 voxels in every direction. Maximum field inhomogeneity was assigned for the sinus cavity to achieve maximum gradients of 5, 15, 25, 35, and 45 Hz/cm; inhomogeneity for the ear canals was half that of the sinus cavity. For all simulations, average global stiffness error was calculated for each data set and compared to the average stiffness of the simulation with no distortion. An undistorted inversion was used as the reference rather than the ground truth stiffness from the simulation to isolate changes to the property maps due to distortion as opposed to changes from other sources of error such as incomplete contrast recovery from regularization required for stability (NLI), and artifacts at mechanical property interfaces due to the local homogeneity assumption (LDI).

EPI: 2D EPI simulations were created with eleven different readout times, from 10 ms to 60 ms, in increments of 5 ms, which was controlled based on the echo spacing. Each simulated trajectory was used to sample the object with different field inhomogeneity described above. After sampling and reconstructing the simulated images, we also applied FUGUE and TOPUP correction separately using FSL[46]. FUGUE utilizes the same fieldmap which was used to create the simulations, downsampled to the lower imaging resolution, while TOPUP uses the simulated AP and PA images for correction. Field correction is applied to the real and imaginary data separately[32], from which image phase was calculated.

Spiral: 2D spiral simulations were created using interleaved, constant-density, spiral-out trajectories[22]. Readout time was controlled by changing the number of interleaved spirals, with more interleaved spirals resulting in a shorter readout time per shot. The number of interleaved spirals were chosen as 14, 12, 10, 8, 6, 4, 3, and 2, resulting in simulated readout times of 7.5 ms, 8.7 ms, 10.4 ms, 12.9 ms, 17.1 ms, 25.5 ms, 34.0 ms, and 50.8 ms, respectively. Data was simulated with each of the spiral trajectories and each of the previously described fieldmaps. Reconstruction was performed for all spiral images both with and without field correction by including field inhomogeneity from the fieldmap in the reconstruction model[28]. Field correction was applied iteratively during image reconstruction using the time segmentation approach, with 9 time segments.

2.2 Phantom Experiments

Phantom experiments were performed to examine effects of distortion in a controlled system. An agarose phantom was designed with a geometry of alternating cubes of different stiffnesses arranged in three dimensions. Agar cubes (Sigma-Aldrich A9799) were created following our previously published protocol[47] and concentrations were chosen to achieve physiologically-relevant stiffnesses of approximately 3.5 (0.8% agar concentration) and 6.0 kPa (1.0% agar concentration). Agar at a concentration of 1.0% was solidified in a rectangular container with rounded corners (12.0 x 12.0 x 12.0 cm^3; approximately 1700 milliliters). After setting, the entire gel was removed from the container and partitioned into 3 x 3 x 3 cm^3 cubes. These 1.0% agar cubes were placed in an alternating fashion in the bottom layer of the phantom and surrounded by 0.8% agarose gel to create an alternating pattern. This process was repeated to create the remaining layers and produce a single continuous phantom of alternating stiffness cubes.

Two MRE experiments were performed on the phantom using a Siemens 3T Prisma scanner with a 64-channel RF-receive coil. The first experiment used an EPI readout with changing bandwidth to control readout time, while the second used a spiral readout with changing number of interleaved shots to control readout time. To provide a distortion-free reference, a standard spin-echo MRE was collected with FOV = 160x160 mm^2, matrix = 80x80, 60 slices, 2.0 mm isotropic resolution, and TE/TR = 65/4800 ms. During MRE acquisition for both experiments, shear waves were generated by vibrating the lower surface of the phantom at 50 Hz using a flat, rigid pneumatic driver (Resoundant, Rochester, MN, USA). All MRE scans were performed after the phantom was allowed to reach room temperature.

EPI: Experiment 1 included a set of scans acquired with a 2D single-shot spin-echo EPI MRE sequence with imaging parameters including: FOV = 240x240 mm^2, matrix = 120x120, GRAPPA R = 3, 60 slices, and 2.0 mm isotropic resolution, and TE/TR = 106/10800 ms. Five scans were performed with varying readout times of 28.0 ms, 29.2 ms, 37.2 ms, 44.4 ms, and 56.8 ms achieved by changing imaging bandwidth (1948, 1602, 1226, 992, 758). Each of the five EPI scans took 5:13 to acquire. Additionally, a gradient-echo fieldmap of the same matrix size, resolution, and FOV was acquired with TE1/TE2/TR as 5.75/8.21/492.0 ms. For each EPI scan, two additional auxiliary scans with phase encode direction in AP and PA were collected with no MRE motion encoding. Distortion correction was performed on each EPI scan with FUGUE using the collected fieldmap and with TOPUP using the auxiliary scans with opposing phase encode direction.

Spiral: Experiment 2 included a set of scans acquired with a 2D spiral MRE sequence[23] with an adjustable number of interleaved, constant-density spiral readouts[22]. Image parameters included FOV = 160x160 mm^2, matrix

= 80x80, 60 slices, 2.0 mm isotropic resolution, and TE/TR = 60/7200 ms. The scans were performed with readout times of 6.3 ms, 7.6 ms, 9.4 ms, 12.5 ms, 18.6 ms, 37.1 ms, and 74.0 ms, achieved through interleaved numbers of shots 12, 10, 8, 6, 4, 2, and 1. Each scan took a variable length of time proportional to the number of interleaved shots, with scan times ranging from 2:53 to 17:17. Additionally, a spin-echo fieldmap was collected with the same FOV and resolution and TE1/TE2/TR = 15/16/2220 ms, which was also used to calculate coil sensitivity maps for iterative SENSE image reconstruction[48].

The spin-echo MRE scan was used as the undistorted reference for all analyses of the phantom data. Each EPI and spiral MRE scan was registered to the reference scan using FSL FLIRT[49], and manual masks of each of the 64 phantom cubes were created from the reference image as the regions-of-interest. The masks were used to determine average stiffness of each cube, as well as the average field inhomogeneity from the corresponding fieldmap.

2.3 *In vivo* Brain Experiments

In vivo brain experiments with EPI and spiral imaging were conducted on healthy adult participants using a Siemens 3T Prisma scanner with a 64-channel head RF-receive coil. For each MRE experiment, 50 Hz vibrations were delivered to the head via pneumatic actuator system with passive pillow driver system. Each set of experiments included a high-resolution anatomical T_1-weighted MPRAGE for anatomical localization (0.9 x 0.9 x 0.9 mm^3; TE/TI/TR = 2.32/900/2300 ms). This study was approved by the University of Delaware Institutional Review Board and all participants gave informed written consent prior to being studied. Imaging time constraints for human subjects did not allow the spin-echo sequence to be used as an undistorted reference.

EPI: Four healthy adult participants (1 male / 3 female; age 22-27) completed EPI MRE experiments following the same experimental design as described for the phantom experiment. Average stiffness values were computed across each stiffness map and compared to the average stiffness value at the shortest readout time (28.0 ms) which was considered the least distorted image.

Spiral: Five healthy adult participants (2 male / 3 female; age 21-25) completed the spiral MRE experiments which included data collected with a 3D multiband, multishot spiral MRE sequence[50]. This sequence uses a multiband RF pulse to excite multiple volumes, samples the 3D k-space as a stack of interleaved in-plane spiral readouts, and includes a navigator echo for motion-induced phase error correction. The spiral sequence parameters included: FOV = 240x240 mm^2, matrix = 150x150, 64 total slices, TE/TR = 76/1400 ms, and 1.6 mm isotropic resolution. Readout time was controlled through the number of interleaved spiral shots, N = 2, 4, 6, and 8 shots, corresponding to readout times of 37.3 ms, 18.7 ms, 14.8 ms, and 9.3 ms, respectively. Each spiral scan included a separately collected spin-echo fieldmap with TE1/TE2/TR = 15.0/15.9/50.0 ms. Image reconstruction was performed both with and without field correction using an iterative algorithm in PowerGrid, which is a GPU-based reconstruction platform[51]. The stiffness maps from all scans were registered to the scan with 8 interleaved spirals (9.3 ms readout), considered to be the least distorted scan as a reference, and percent difference was calculated

Accepted Manuscript
Version of record at: https://doi.org/10.1002/nbm.4616

globally. In addition, segmentations were performed using regions from the Harvard-Oxford Cortical and Subcortical Atlases[52], which identifies each of 48 cortical structures and the 21 subcortical gray matter structures and brain stem. This segmentation was performed by first registering the 1 mm MNI template to the anatomical MPRAGE scan using FSL FNIRT[53] then to the MRE data using FSL FLIRT[49].

3. RESULTS

3.1 Simulation Results

Figure 1 shows results of simulated distortion in EPI and the effects on calculated stiffness from both NLI and LDI. Positive off-resonance gradients in the phase encode direction cause a stretching of the image and an overestimation of stiffness, whereas gradients in the opposite direction cause a compression of images and an underestimation of stiffness. As the EPI readout time increases, or the gradient of the fieldmap increases, the resulting stiffness error increases. This trend holds true for inverting displacement data using both NLI and LDI. The results for NLI can be seen quantitatively in Figure 2, where even at a reasonably short readout time of 20 ms, error at high field inhomogeneity (64 Hz/cm) is as large as 0.91 kPa (33.7%) without correction. This error becomes considerably larger at longer readout times, with up to 115% error at readout time of 40 ms. With opposite off-resonance gradient direction, at the same parameters of 20 ms readout time and 64 Hz/cm, the global error is 18.1%. This comparatively lower error when the object is compressed is sustained for all short readout times, and for some long readout times, provided they are at small field inhomogeneities. (See Supplemental Figure S3 for full quantitative NLI results).

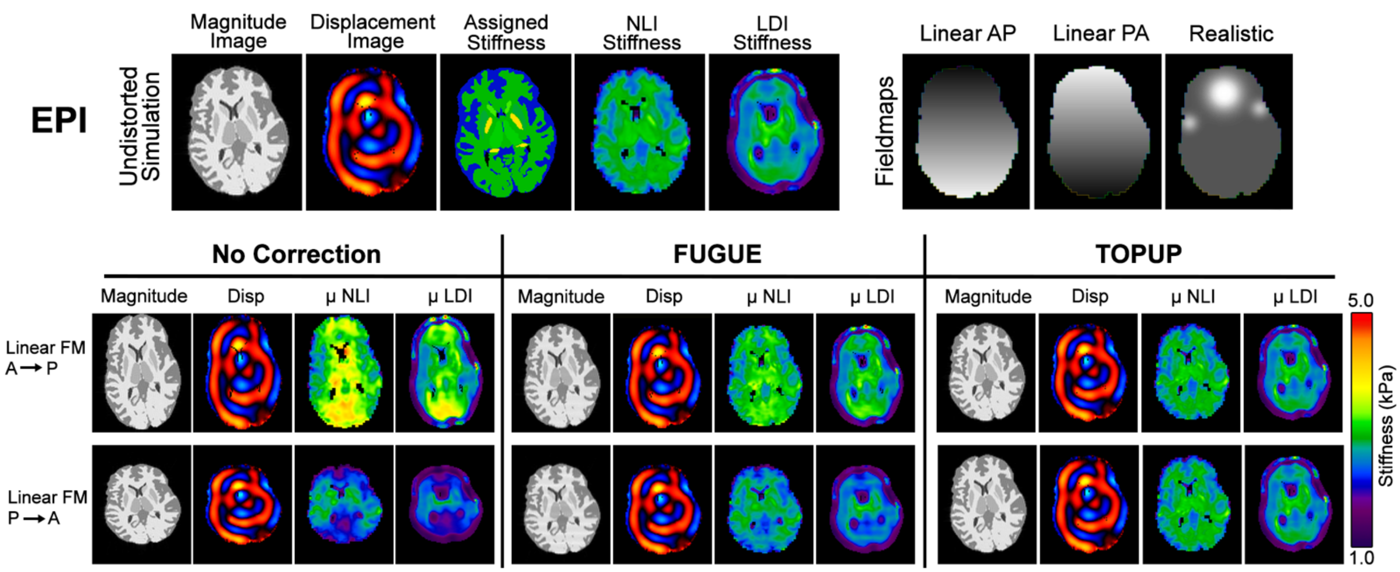

Figure 1: MRE EPI simulation experiments. Simulations were reconstructed accounting for field inhomogeneity gradients and resulting magnitude, displacement, and stiffness (μ) images are shown. The linear fieldmaps have a 24 Hz/cm gradient. Images are shown with k-space phase encoding in the AP direction and fieldmap gradients in both AP and PA with a readout time of 30.0 ms. Post-processing was done using FUGUE correction and TOPUP correction.

Figure 2 also demonstrates the effects of the EPI distortion correction techniques FUGUE and TOPUP when using the NLI inversion. FUGUE and TOPUP both work well for correcting error at short readout times, and the resulting images from both techniques have less than 10% residual error when using an NLI inversion for a readout time of 20 ms even at the largest field inhomogeneities, with TOPUP outperforming FUGUE at small to medium levels of distortion. However, in situations with very large distortion, either from larger inhomogeneities or longer readout times, TOPUP is unable to correct images and appears to be unstable. For these large distortions, FUGUE surpasses TOPUP in performance, with remaining errors using FUGUE of only around 11.5% even at long readout time of 40 ms and large gradients of 64 Hz/cm.

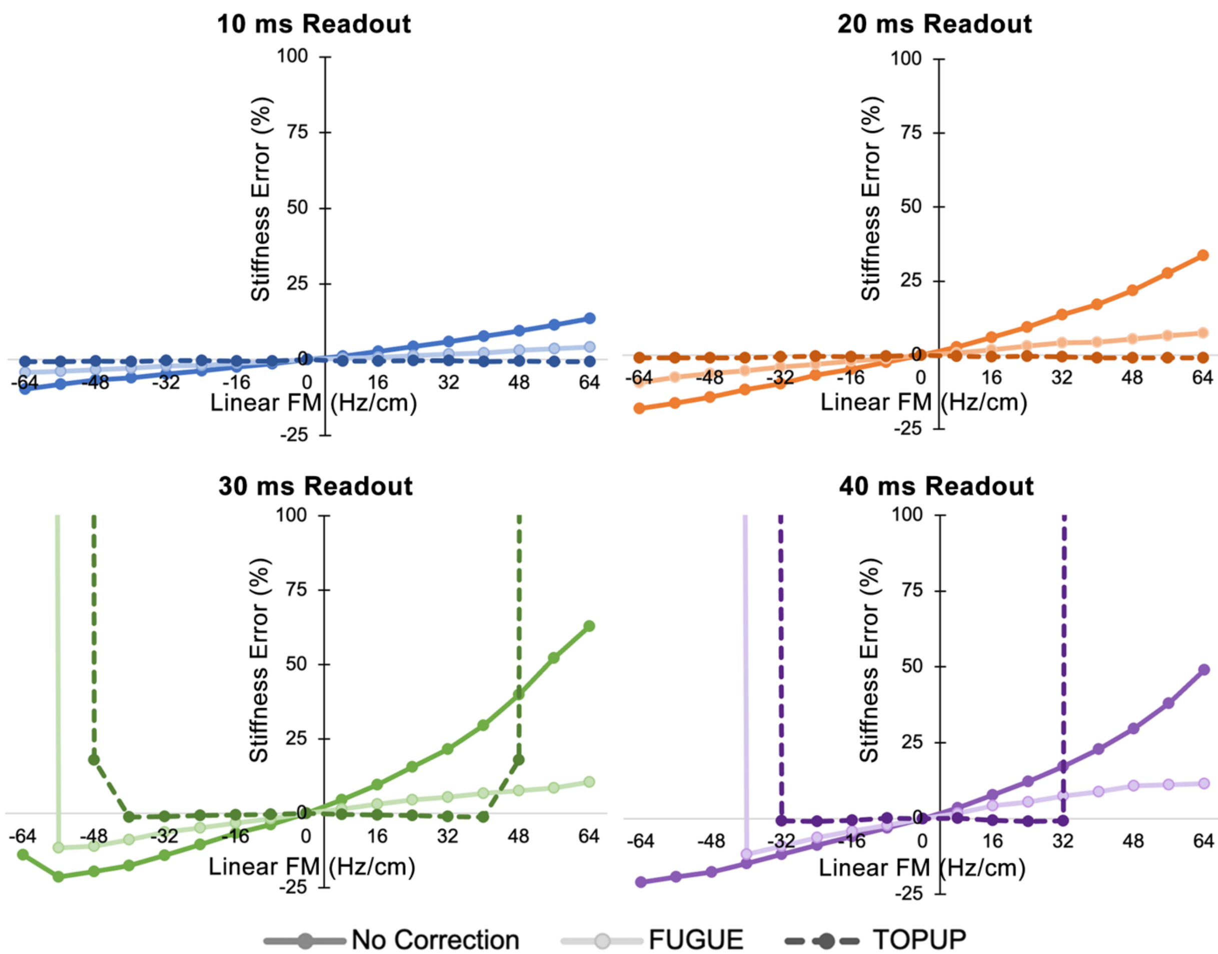

Figure 2: Quantitative results of MRE simulations reconstructed with various off-resonance gradients applied (-64 Hz/cm to 64 Hz/cm) and inverted using NLI. EPI readout times between 10 ms and 40 ms were used, and with FUGUE and TOPUP correction applied.

Field gradients which are not in the phase encode direction, such as in the readout or slice direction, have similar effects on stiffness in that errors increase with greater readout time and field inhomogeneity (Supplemental Figures S5 and S6). However, specific patterns of error in the presence of these off-resonance gradients vary based on direction. While the gradients in the phase encode direction caused a stretching and compressing of the wave image, the readout and slice select gradients result in an image shearing effect. Gradients in the readout direction resulted in some brain regions being overestimated in stiffness, and others being underestimated in stiffness, with the inverse stiffness patterns for opposite off-resonance direction. Distortion which resulted in shearing in the slice direction always produced an overestimate of stiffness, regardless of sampling direction, and these uncorrected z-direction off-resonance gradients resulted in the largest errors of any of the three gradient directions. However, following field correction, z-direction slice shearing exhibits the lowest error, even at the highest levels of distortion (all less than 3% error). Residual error from distortion in all directions after FUGUE correction appears proportional to the original error from distortion. In general, TOPUP works well to correct error at short readout times and is unstable at high distortion. All simulations with off-resonance gradients in each direction, both with and without correction, can be found in Supplemental Figures S5 and S6, respectively.

Figure 3 shows the results of the MRE simulation with spiral sampling and the effect of interleaved spiral shots on stiffness errors. When using NLI, at field inhomogeneity of 24 Hz/cm, a two-shot spiral with readout time of 50.8 ms leads to a large stiffness error of 191.8%, while an eight-shot spiral with readout time of 12.9 ms has only 8.9% error. The single-shot spiral will cause such large distortion in the presence of large off-resonance gradients that the data becomes entirely corrupted because NLI cannot find a physically realistic property distribution to fit the data. Figure 4 shows quantification of this error at different levels of field inhomogeneity; even with more reasonable distortion levels (8 Hz/cm), two shots results in a 12.3% error while eight shots result in just 0.8% error, without correction. Field inhomogeneity correction in spiral imaging performed by applying the fieldmap during iterative reconstruction serves to greatly improve distortion and reduce error. Up to off-resonance gradients of 32 Hz/cm, in all trajectories, we observe less than 2% residual error after correction when using NLI. In all cases, increasing the number of interleaved shots and thus shortening the readout time reduces mechanical property error, both with and without correction[28] (see Supplemental Figure S10 for images).

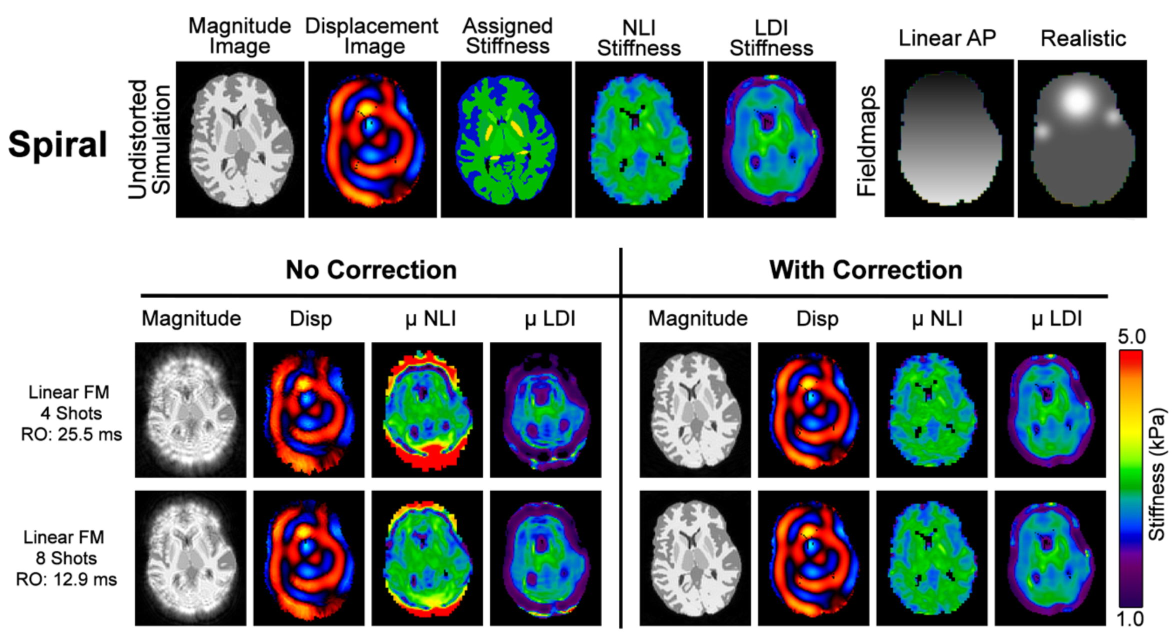

Figure 3: MRE spiral simulation experiments. Simulations were reconstructed accounting for field inhomogeneity gradients and resulting magnitude, displacement, and stiffness images are shown. Images are shown for k-space

sampling using four interleaved shots (25.5 ms readout (RO)) and eight interleaved shots (12.9 ms readout). Results are shown for each image reconstructed with and without iterative correction during image reconstruction.

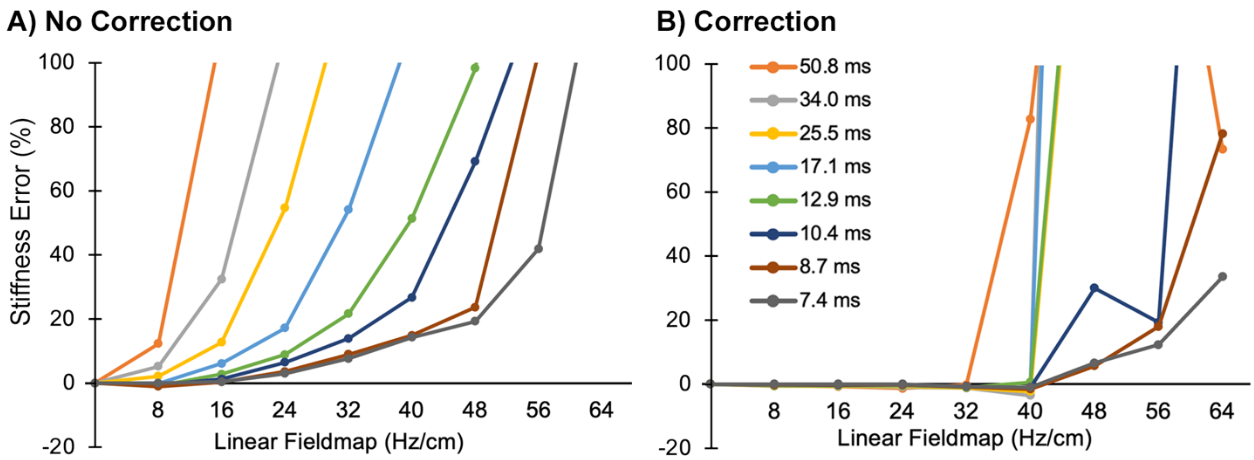

Figure 4: Error in estimated stiffness with NLI from MRE simulations with spiral k-space sampling and linearly increasing field inhomogeneity gradients with 2, 3, 4, 6, 8, 10, 12, and 14 interleaved spirals. Results are shown A) without and B) with field correction.

As with linear gradients, error results from long readout times and large field gradients in both EPI and spiral readouts. However, in realistic fieldmap patterns, the direction of average stiffness error is less identifiable, as gradients appear in all directions and thus images contain both areas of overestimated and underestimated stiffness. For simulations with EPI sampling, FUGUE and TOPUP provide correction, but it is less effective for the realistic fieldmap than for the linear fieldmap. In the spiral simulations with realistic fieldmaps patterns, the spatial blurring effect is prominent in stiffness map, which is improved via use of the fieldmap during reconstruction (see Supplemental Figure S12 and S14 for images).

Using LDI as the method for simulation inversion we see many of the same trends as in NLI, with stretched wavefields leading to overestimates of stiffness and compressed wavefields leading to underestimates of stiffness. Longer readout times and larger off-resonance gradients similarly resulted in higher error. FUGUE and TOPUP likewise served to reduce stiffness errors and began to fail to return improved stiffness maps at very high distortion, as seen with NLI, suggesting that the underlying wavefield is fundamentally changed in these cases. One notable difference between the NLI and LDI inversions is in the spiral images where field inhomogeneity results in image blurring, as LDI underestimates stiffness while NLI overestimates stiffness; however, the absolute error is similar between the two for both uncorrected and corrected images. See Supplemental Section Figures S4, S7-11, and S13-14 for complete LDI results.

3.2 Phantom Results

Figure 5 shows a cross-sectional view of the estimated stiffness of the agarose phantom, imaged with EPI at different readout times, both with and without field correction. Using the distortion free spin-echo MRE scan as the reference, it is seen that a readout time of 44.4 ms produces a global error of 82.0%, with readout time of 56.8 ms returning stiffness maps that were completely unusable. The shorter readout times have progressively smaller global error of 25.8%, 9.6%, and 8.7%, at times of 37.2 ms, 29.2 ms, and 28.0 ms, respectively. As in the simulations, FUGUE and TOPUP are both able to improve the stiffness errors. At 44.4 ms readout FUGUE correction results in just 5.0% global error, down from 82.2% error without correction. At this long readout time, in the most distorted cube, FUGUE correction improves stiffness error from 572.1% to 34.4%. TOPUP correction is also effective, and for the same data set results in 15.0% global error for readout time 44.4 ms (from 82.2% without correction). The error seen in each cube is related to the average field inhomogeneity in that region, as seen in Figure 5B. Increases in stiffness error correspond with the greater field inhomogeneity across the cubes, with more of an effect at longer readout times, and FUGUE and TOPUP work well to correct this error regionally at all levels of distortion. Supplemental Figure S16 shows the corresponding magnitude images for all phantoms; at longer readout times the geometry of the phantom is warped, which is improved with each of the correction methods.

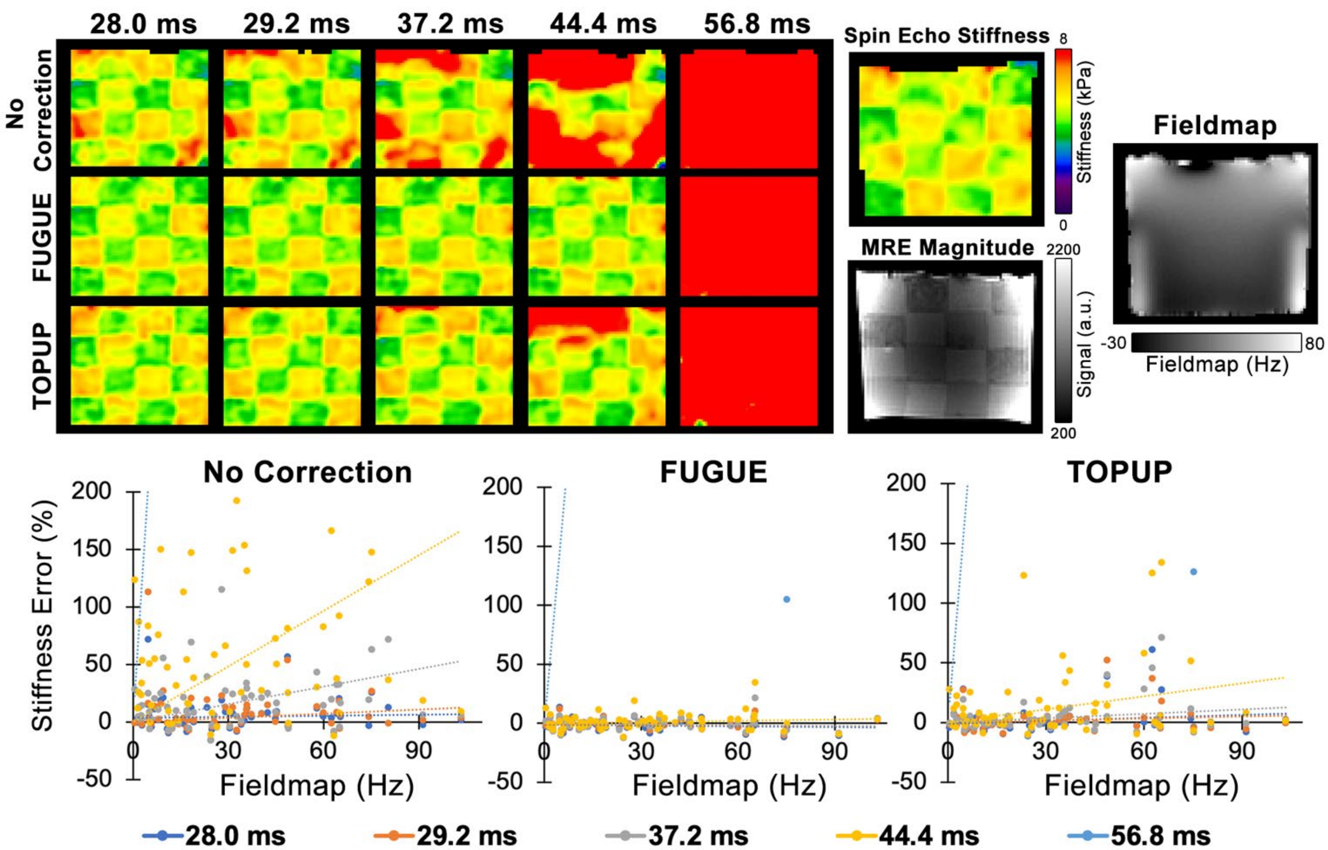

Figure 5: A) NLI stiffness maps from EPI phantom experiment at five different readout times (28 ms to 56.8 ms), each with FUGUE and TOPUP correction, demonstrating increased error in stiffness maps with longer readout times, and improvements using either of the field correction methods. Corresponding fieldmap, MRE magnitude, and corresponding distortion free spin-echo stiffness images pictured. B) Comparison of stiffness error and field inhomogeneity, with each cube as a separate region, and stiffness from all readout times compared to stiffness from the distortion-free spin-echo MRE scan.

Figure 6 presents the phantom results when imaged with a 2D spiral readout and using the number of interleaved shots to control the readout time. Single shot images reconstructed without correction produced extensive errors in stiffness, with global error of 218.4% from the reference for a readout time of 74.0 ms. Increasing the number of shots to two, for a readout time of 37.1 ms, substantially reduces this error, with resultant global stiffness error of 0.9%, and the maximum error in any single cube being 9.6%. Average error becomes progressively less with more interleaved shots. With correction, nearly all readout times showed improvement in average stiffness error, with one shot resulting in errors of just 4.4% and two shots having error of 0.7%.

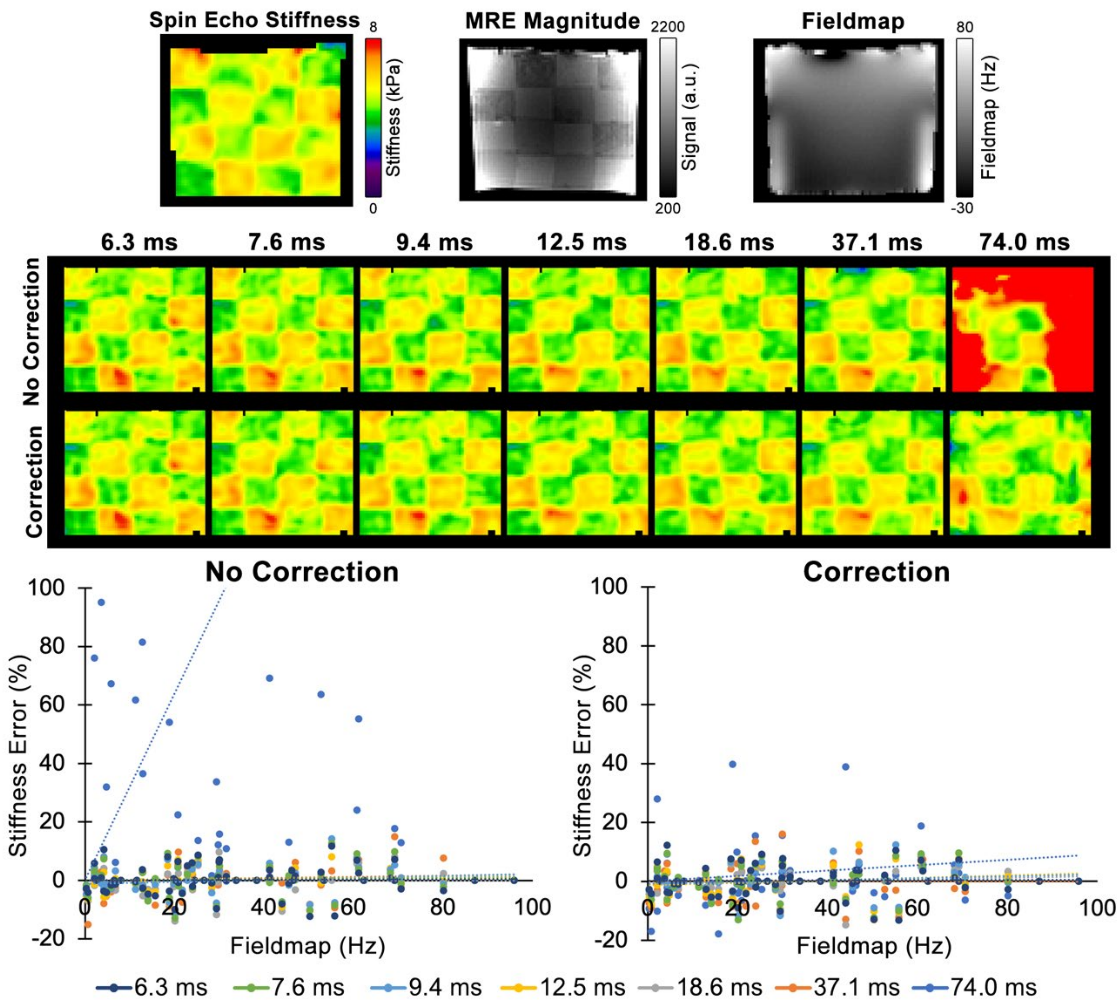

Figure 6: A) NLI stiffness maps from spiral phantom experiment at seven different readout times (6.3 ms to 74.0 ms), each with and without field correction during reconstruction, demonstrating increased error in stiffness maps with longer readout times, and improvements using field correction. B) Comparison of stiffness error and field inhomogeneity, with each cube as a separate region, and stiffness from all readout times compared to stiffness from the distortion-free spin-echo MRE scan.

Using LDI, we see very little differences between the final stiffness maps at each of the readout times, or when using correction methods (Supplemental Figure S15 and S17). For EPI, aside from readout time of 56.8 ms, which suffers from the same data corruption as with NLI, changing readout times produced at most a 2.76% average error from the reference. Likewise, no meaningful improvements were seen with FUGUE or TOPUP correction methods, and these correction methods actually resulted in slightly higher levels of error for all readout times. Local direct inversion showed a similar trend for the spiral phantom, where, aside from the longest readout time of 76.0 ms, stiffness maps appear qualitatively very similar and showed no consistent patterns of improvement with decreases in readout time. Further, stiffness errors were only improved for readout time of 76.0 ms when reconstructed with field correction and all other readout times showed no meaningful quantitative improvements. We note however, for both EPI and spiral sampling, that the phantom stiffness estimates from LDI are consistently poor compared to the true geometry, even in the undistorted reference case. Violation of the local homogeneity assumption in LDI at material interfaces causes large artifacts at stiffness interfaces, and it is difficult to see the effect of distortion on top of this very large baseline error.

3.3 In Vivo Results

Figures 7 and 8 show the results from the *in vivo* EPI experiment, which was conducted to confirm the effects of distortion observed in simulations and in phantoms. As expected, there exists similar high stiffness error at long readout times; for example, a readout of 56.8 ms leads to a whole brain stiffness error of 6.6% across all subjects, whereas readout times of 44.4 ms, 37.2 ms, and 29.2 ms give whole brain stiffness errors of 5.2%, 1.1%, and 0.38%, respectively. In addition to error in average stiffness, in areas of high off-resonance gradients, long readout times result in signal cancellation which is sufficiently severe to have parts of the image entirely corrupted. FUGUE and TOPUP do appear to correct the magnitude image geometry (Figure 7), however they do not successfully correct average stiffness values and even made the property estimates worse. FUGUE made the average stiffness values up to 0.7% worse and TOPUP made the data between 0.2% and 0.5% worse across all readout times. This is true when using the readout time 28.0 ms without correction as the reference, or with either type of correction as the reference. While FUGUE and TOPUP correction can recover the magnitude images, they are unable to recover magnitude or phase data in areas which were entirely corrupted by distortion leading to permanently lost data. OSS-SNR ranged between 8.6 and 13.6 across the five scans with no consistent pattern or decrease seen with increasing readout time, indicating SNR effects were not responsible for the observed errors.

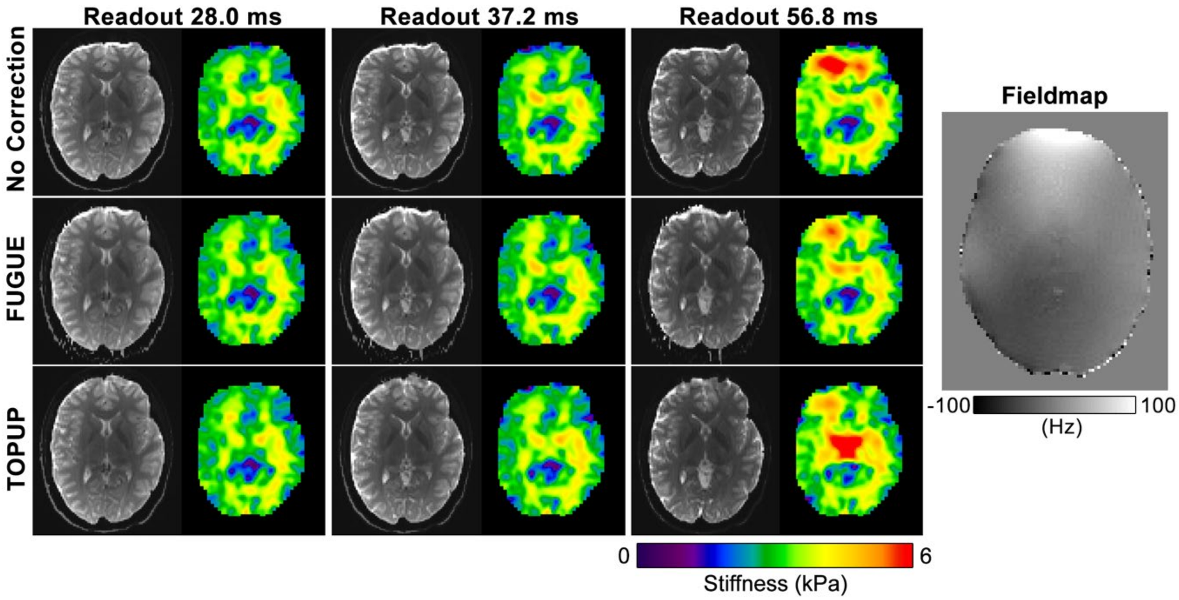

Figure 7: Results of the in vivo EPI experiment using NLI for one representative subject with three representative readout times (28.0 ms, 37,2 ms, and 56.8 ms), and the corresponding field map. Stiffness increases with readout time and is not completely corrected with FUGUE or TOPUP.

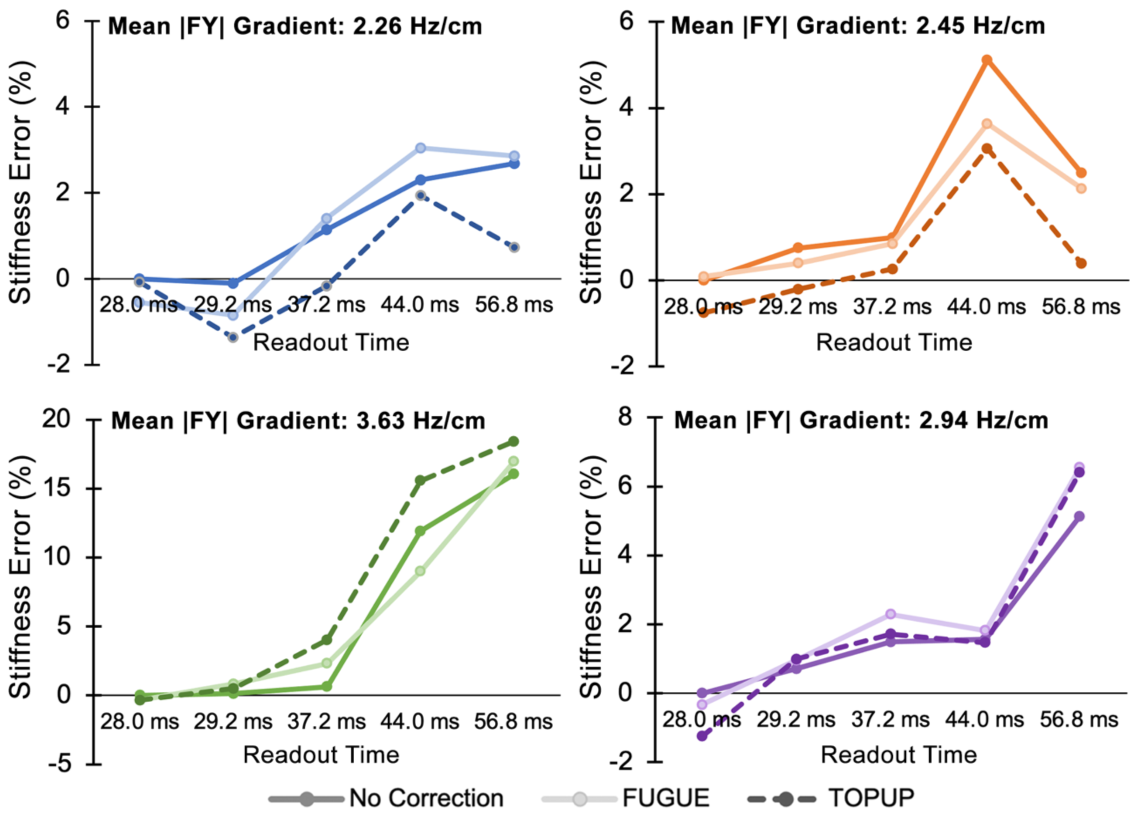

Figure 8: Percent stiffness error from NLI relative to the least distorted image for in vivo brains with five readout times (28.0 ms to 56.8 ms). Each panel is a different subject, with the average y-direction gradient noted. In all cases, stiffness error increased with readout time, and was only partially corrected by FUGUE or TOPUP.

Using the spiral sequence, we again see that progressively longer readout times lead to larger stiffness error. With an 8 shot interleaved spiral as the least distorted case, we see that the 2, 4, and 6 shot spiral cases resulted in 7.2%, 2.7%, and 1.7% error, respectively, with each case resulting in an overestimate of calculated stiffness (Figure 9). Increases in readout time led to blurring of the magnitude image, and thus a blurring of the phase images used to calculate displacement, which ultimately affects property estimates. With field correction we found average global stiffness is not significantly affected, but regional properties are affected by local blurring (Figure 10). The subcortical structures closest to the brain stem showed the most regional error, and the amygdala, hippocampus, and thalamus have the largest errors at long readout times without correction. Iterative correction improves the error seen in nearly all structures at the readout times of 14.8 ms and 18.7 ms (6 shots and 4 shots, respectively). However, with the longest readout time of 37.3 ms (2 shots), correction did not improve calculated stiffness values (Table 1). A complete table of error for all the subcortical and cortical atlas regions can be found in the Supplemental Section Table S1. OSS-SNR ranged between 9.18 and 10.19 across the five scans with no consistent pattern or decrease seen with increasing readout time.

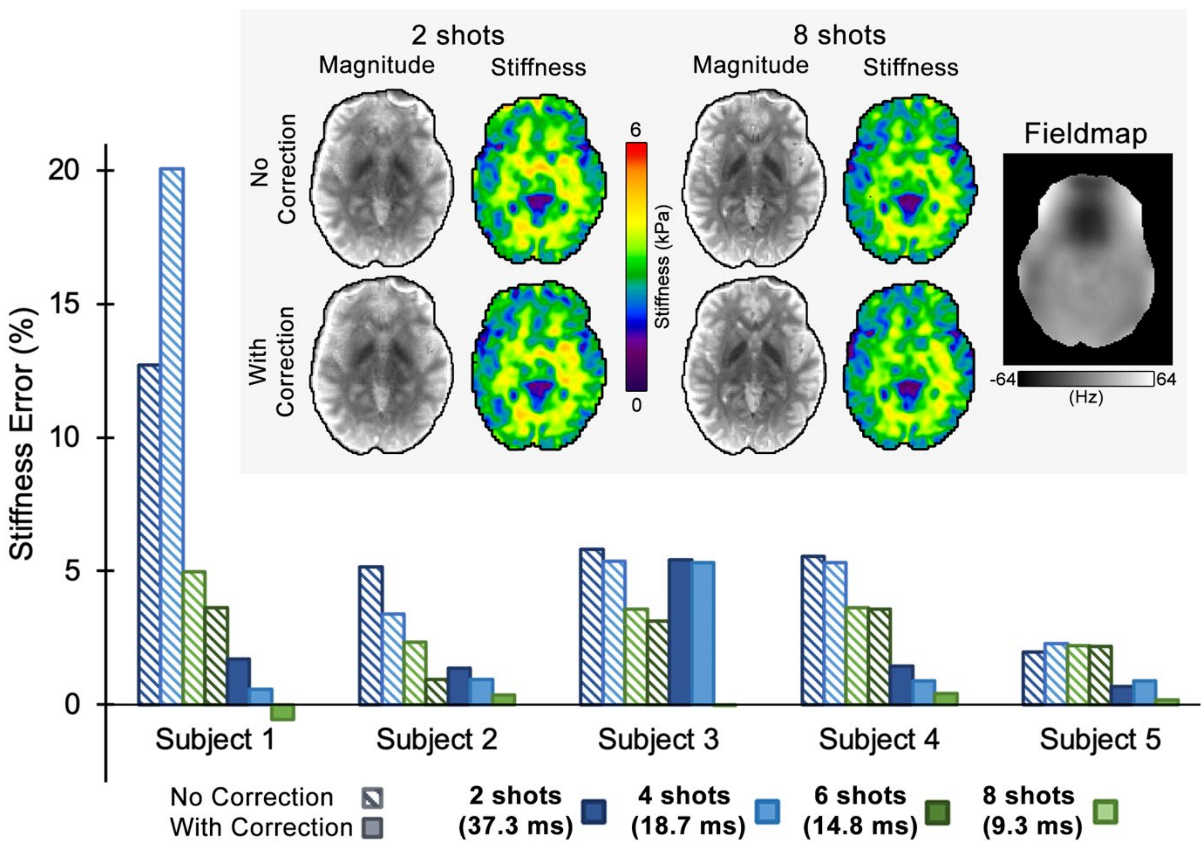

Figure 9: In vivo brain experiment with spiral k-space sampling at 1.6 mm isotropic resolution. Shear stiffness images from NLI and data for 2, 4, 6, and 8 interleaved spirals, used to control readout time (37.3 ms, 18.7 ms, 14.8 ms, 9.3 ms). Results are shown with and without iterative correction during image reconstruction.

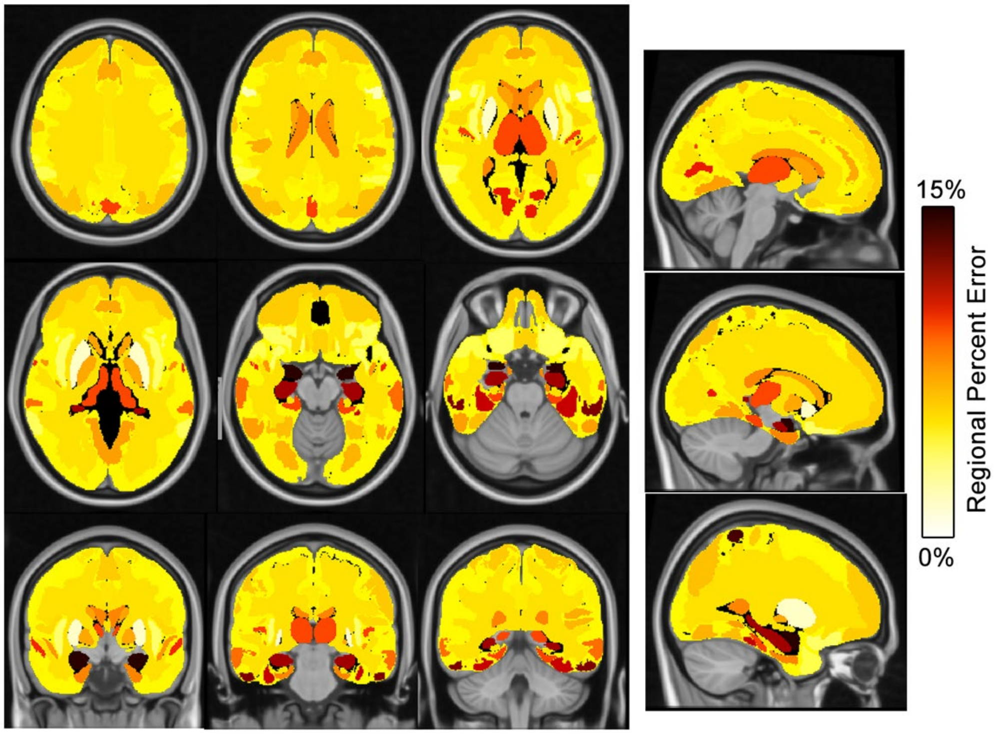

Figure 10: Regional percent error in stiffness from geometric distortion, using NLI, between a readout time of 37.3 ms and 9.3 ms averaged across five subjects for each of the structures in the Harvard-Oxford Cortical and Subcortical Atlases.

Table 1: Percent stiffness error, and standard deviations from distortion for six subcortical gray matter structures using NLI, at readout times of 14.8 ms, 18.7 ms, and 37.3 ms compared to a readout time of 9.3 ms averaged across five subjects, with and without field correction. See Supplemental Table S1 for a complete list of the percent distortion in each of the Harvard-Oxford cortical and subcortical atlas regions.

Region	**No Correction- Stiffness Error, % (Stdv)**			**With Correction - Stiffness Error, % (Stdv)**		
	14.8 ms	*18.7 ms*	*37.3 ms*	*14.8 ms*	*18.7 ms*	*37.3 ms*
Amygdala	**4.67** (2.69)	**10.39** (3.23)	**11.89** (2.39)	**0.17** (1.69)	**9.66** (3.13)	**12.43** (5.35)
Hippocampus	**5.10** (3.27)	**6.86** (3.08)	**8.23** (7.65)	**2.43** (0.59)	**6.89** (6.39)	**8.37** (3.02)
Thalamus	**5.04** (1.54)	**7.97** (0.09)	**6.98** (0.96)	**4.61** (3.13)	**7.33** (3.10)	**10.08** (2.29)
Caudate	**2.54** (0.43)	**3.82** (4.11)	**6.96** (2.99)	**1.85** (0.76)	**3.56** (3.30)	**9.17** (2.31)
Pallidum	**4.88** (0.20)	**4.61** (0.58)	**5.22** (1.33)	**5.47** (1.33)	**4.16** (1.69)	**7.73** (1.82)
Putamen	**2.61** (0.37)	**2.48** (1.19)	**3.55** (0.75)	**2.16** (1.26)	**2.44** (4.32)	**5.70** (0.03)

4. DISCUSSION

We have presented an analysis of the quantitative effects of off-resonance related geometric distortion on mechanical property calculation in MRE and have demonstrated how distortion affects images from both EPI and spiral *k*-space readouts, with resulting errors dependent on readout time and strength and direction of the field inhomogeneity gradients. Further, we evaluated the effectiveness of traditional distortion correction techniques on calculated mechanical properties and showed that they can reduce error in stiffness images, though limits exist in cases of greater distortion. Through this work we aim to inform pulse sequence design to improve the accuracy and reliability of MRE data, particularly as fast, high-resolution MRE imaging becomes increasingly popular and necessary for clinical translation.

MRE data is uniquely susceptible to influence from off-resonance geometric distortion. Mechanical properties are calculated from imaged wavefields by inverse solution of the equation describing harmonic vibration of an isotropic, viscoelastic material, which assumes an undistorted geometry. Geometric distortion deforms the displacement fields such that the effective wavelength is changed in certain directions, ultimately resulting in inaccurately calculated mechanical properties. In a sequence with Cartesian *k*-space sampling, such as an EPI sequence, pixel shift can be defined as $\Delta r_{pe}(x,y,z) = \gamma \Delta B_0(x,y,z) T_{ro}$, where γ is gyromagnetic ratio, ΔB_0 is the magnetic field inhomogeneity, and T_{ro} is the data readout time, and the corresponding distortion is calculated as the gradient of the pixel shift map, $d\Delta r_{pe}/dy$[54]. Using this equation to understand the results from our simulation, we found that distortion can cause rapidly increasing errors in stiffness, such that when images are stretched, 1% distortion leads to negligible NLI stiffness error of only 0.1%, whereas 7% distortion leads to approximately 7% stiffness error, and 15% distortion leads to approximately 20% stiffness error. Interestingly, when the off-resonance gradient is in the opposite direction, such that wavelengths are being compressed, there is a distortion limit past which NLI is unable to successfully reconstruct image mechanical properties due to excessive model-data mismatch causing the algorithm to diverge as it cannot find a realistic stiffness distribution to fit the corrupted data. In practice, these effects are more complicated as off-resonance gradients in the brain exist simultaneously in all directions, thus images can stretched, compressed, blurred, or sheared, and MRE shear waves will travel in all directions[55,56], making the property estimate errors arising from distortion variable across the brain and between individuals.

Both magnetic field inhomogeneity gradients and data readout time affect distortion, and it can be difficult to reduce these effects. Field inhomogeneity gradients arising from tissue susceptibility cannot be adjusted because long readout times are often necessary for achieving high-resolution data in a short scan time. The EPI distortion correction utilities of FUGUE and TOPUP can be applied to MRE data by calculating regional severity of off-resonance gradients and transforming the real and imaginary parts of the MRE complex signal separately[32]. Here, we have found in simulation that FUGUE and TOPUP present their own strengths in correction of MRE mechanical properties. FUGUE appears to proportionally correct images at all levels of distortion studied, such that an image which is highly distorted will have stiffness errors greatly reduced from correction, though this will be incomplete. Interestingly, FUGUE correction appears to work less well for the wave-compression cases, which is agreement with findings from correction of diffusion tensor imaging (DTI) data[57]. TOPUP, however, provides excellent correction of images with minimal stiffness error, but only up to a certain amount of distortion, past which the correction fails, and it returns highly inaccurate results. Fehlner et al., previously demonstrated qualitative improvement to MRE images when using TOPUP[32]; here we have quantified this performance and discovered limits to the correction. While results in the phantom and *in vivo* brain generally agree with the simulations of EPI sequences, where longer readout times resulted in increasing stiffness error, both FUGUE and TOPUP correction yielded less effective stiffness correction in the brain than in simulation or in the phantom, which could be attributable to subject movement during collection of the fieldmap scans.

Spiral *k*-space readouts face many of the same challenges as EPI in terms of distortion from field inhomogeneities. However, in spiral imaging, all high frequency data is collected at the end of the readout time, when the off-resonant spins are most dephased, and thus distortion presents as a spatial blurring[58]. The blurring observed in the magnitude image also affects the phase image and therefore the estimated mechanical properties; in simulations, phantoms, and *in vivo* brains, greater blurring led to larger stiffness error. In the brain, we found error in global mechanical property values that were greater with increased readout time as well as localized errors in areas of higher field inhomogeneity. Correction of *in vivo* data during reconstruction both visibly improves blurring in the magnitude image and therefore reduces regional stiffness error, though it has minimal effect on global properties. These differences may not be due only to field inhomogeneity as increasing the number of interleaved spirals may also decrease the effects of motion-induced phase error[19], as more shots reduce the deleterious effects of phase errors in any one shot, though we did not observe differences in OSS-SNR between scans. We also note that at the longest readout time tested (37.3 ms from two spiral shots), correction did not improve stiffness and even made errors worse in some regions, pointing to a limit to correction at the greatest readout times or field inhomogeneities. Improvements in performing field correction during image reconstruction have recently been proposed, including the use of model based approaches and low rank encoding operators for increased correction efficiency while maintaining accuracy of correction, which will serve to greatly decrease computational load and times for reconstruction of spiral images with correction[59,60].

The inversion method used, LDI or NLI, results in similar patterns of distortion related error in simulation, however in the phantom and *in vivo* they present different trends. NLI appears to be more sensitive to readout time and correction mechanisms, whereas LDI returns nearly identical stiffness maps in the phantom and *in vivo* for the differing readout times and after correction is applied. This may be due to the local homogeneity assumption in LDI, which could cause the algorithm to be not particularly responsive to image distortion and corrections, as these effects are small compared with the larger artifacts resulting from the spatial homogeneity enforcement. On the other hand, NLI does not rely on the local homogeneity assumption and appears to return spatially resolved property maps in the case of ideal data; however, NLI is more sensitive to model-data mismatch when the imaged wave patterns are distorted relative to the true displacements.

Moving to high-resolution MRE is a necessary step towards answering questions in neuroscience about the role of brain stiffness in aging, disease, and neural function, and providing maximum utility in a clinical setting. However, high-resolution sequences naturally require greater data sampling and thus must be designed responsibly to avoid excessive influence from geometric distortion. It is not uncommon in MRE to determine significant group differences in properties between 5-10%[8,61] and individual differences in properties have been related to cognitive function[62–64], thus errors of this order arising from distortion can obscure meaningful effects. Reducing readout time through interleaved trajectories is effective in spiral imaging or when using interleaved EPI, but increases total scan time. Thus, single-shot sequences are popular for clinical MRE studies due to short scan time but are limited in resolution due to distortion. Additionally, parallel imaging techniques can reduce readout time even in single-shot sequences, and advanced sparse sampling methods may allow for further reduction in the amount of collected data to best recover accurate mechanical properties. In this work, we used our 3D multiband, multishot spiral sequence[50] for *in vivo* experiments, which combines interleaved in-plane spiral sampling, 3D slab sampling for high SNR efficiency, and parallel imaging to reduce both readout time and total scan time, ultimately allowing for higher spatial resolution in a reasonable time. Future MRE sequence design should further seek to balance these competing considerations.

Regardless of sequence used or specific application, we recommend adopting an MRE protocol to limit geometric distortion and perform correction to minimize error in property maps. For EPI sequences, readout times less than 30 ms are suggested, with parallel imaging or a segmented trajectory to keep readouts short in high-resolution acquisition. TOPUP appears superior for small to medium levels of distortion, while FUGUE may work well for all levels of distortion; in practice, this choice may be based on acquisition protocol and with care taken to minimize motion between scans. For spiral MRE, readout times should be kept as short as 15-20 ms, and as short as possible for examining structures near regions of high field inhomogeneity, though with consideration for tradeoffs in total scan time depending on the specific sequence adopted. Iterative reconstruction of spiral images should incorporate a fieldmap to reduce blurring effects and stiffness errors. This approach can be used for any MRE sequence reconstructed iteratively, including EPI, and will likely improve results if moderate readout times are used. We note that these recommendations are for data collection on a 3T scanner; it is expected that longer readout times would be acceptable on a 1.5T scanner, but that future data collection at 7T or higher field strength would require even shorter readout times. When designing new MRE protocols, the experiments in this paper can be replicated to understand expected error from off-resonance effects.

This study aimed to quantitatively characterize effects of geometric distortion on MRE property maps using simulations, phantoms, and *in vivo* brain experiments, but is ultimately limited in that it was not possible to analyze all possible MRE sequence combinations and available correction methods for use in MRE. Additionally, while this study examined impacts of distortion from off-resonance, we did not consider other sources of distortion, such as from eddy currents[65] or gradient nonlinearities[66], though the effects on stiffness estimates may be similar. We also did not consider the impact of readout time on echo time or intravoxel phase dispersion due to T2* effects that can reduce SNR, and thus concomitantly affect property estimates in addition to distortion. However, our simulation was noise-free, and we observed no clear SNR dependence in the phantom or brain experiments, thus we believe the effects observed here can be primarily attributed to distortion. The combination of all three experiments gives us the fullest understanding of the effects of distortion, but we recognize that each suffer from different limitations. The simulation does not represent the same artifacts that would be found *in vivo*, including effects of subject motion. The off-resonance gradients found in the phantom are different than those found *in vivo*. In the *in vivo* experiment, it was impossible to obtain a truly distortion free data set for comparison as the ground truth due to limitations on reasonable scan times, and therefore the stiffness errors may be underestimated as there is still some error in the baseline data set chosen as reference. Lastly, field inhomogeneities and wave propagation patterns differ between MRE data collection methodologies, therefore quantified effects of geometric distortion are likely to differ slightly between subjects, scanners, sequences, and actuation practices.

5. CONCLUSION

To establish MRE as a reliable clinical tool for sensitively assessing neural tissue health, pulse sequences and analysis pipelines must be developed with the highest possible resolution while avoiding artifacts, such as those from off-resonance geometric distortion. Here we demonstrate that MRE imaging faces unique challenges from geometric distortion, in that off-resonance gradients in all directions affect the imaged wave fields, which directly leads to error in calculated mechanical properties. The combination of increased readout time and strength of the off-resonance gradient determines the severity of error in the calculated data. Sampling pattern and direction affects the specific manifestation of distortion; for example, EPI readouts cause in a stretching or compression of the image in the readout direction, resulting in an overestimate and underestimate of stiffness respectively, whereas spiral readouts present as a spatial blurring of the image, ultimately leading to a loss of resolution and an increase of stiffness when using NLI, and a decrease in stiffness using LDI. Distortion correction tools, originally developed for other imaging modalities, appear to work well for MRE data, though present limits of accuracy at very high levels of distortion. Moving to higher resolution often necessitates longer readout times, therefore accuracy limits presented in this paper should be used to inform MRE sequence and reconstruction design to ensure the minimization of distortion-related errors.

6. ACKNOWLEDGMENTS

This work was supported in part by NIH grants F31-HD103361, R01-AG058853, R01-EB027577, U01-NS112120, the Delaware INBRE Program (P20-GM103446), and the University of Delaware Research Foundation.

7. REFERENCES

1. Muthupillai R, Lomas DJ, Rossman PJ, et al. Magnetic Resonance Elastography by Direct Visualization of Propagating Acoustic Strain Waves. *Science (80-)*. 1995;269(5232):1854-1857.
2. McIlvain G, Schwarb H, Cohen NJ, Telzer EH, Johnson CL. Mechanical properties of the in vivo adolescent human brain. *Dev Cogn Neurosci*. 2018;34(June):27-33. doi:10.1016/j.dcn.2018.06.001
3. Ozkaya E, Fabris G, Macruz F, et al. Viscoelasticity of children and adolescent brains through MR elastography. *J Mech Behav Biomed Mater*. 2021;115(November 2020):104229. doi:10.1016/j.jmbbm.2020.104229
4. Arani A, Murphy MC, Glaser KJ, et al. Measuring the effects of aging and sex on regional brain stiffness with

MR elastography in healthy older adults. *Neuroimage*. 2015;111:59-64. doi:10.1016/j.neuroimage.2015.02.016
5. Sack I, Streitberger KJ, Krefting D, Paul F, Braun J. The influence of physiological aging and atrophy on brain viscoelastic properties in humans. *PLoS One*. 2011;6(9):1-7. doi:10.1371/journal.pone.0023451
6. Hiscox L, Johnson CL, McGarry MDJ, et al. High-resolution magnetic resonance elastography reveals differences in subcortical gray matter viscoelasticity between young and healthy older adults. *Neurobiol Aging*. 2018;65:158-167. doi:10.1016/j.neurobiolaging.2018.01.010
7. Murphy MC, Huston J, Jack CR, et al. Decreased brain stiffness in Alzheimer's disease determined by magnetic resonance elastography. *J Magn Reson Imaging*. 2011;34(3):494-498. doi:10.1002/jmri.22707
8. Murphy MC, Jones DT, Jack CR, et al. Regional brain stiffness changes across the Alzheimer's disease spectrum. *NeuroImage Clin*. 2016;10:283-290. doi:10.1016/j.nicl.2015.12.007
9. Wuerfel J, Paul F, Beierbach B, et al. MR-elastography reveals degradation of tissue integrity in multiple sclerosis. *Neuroimage*. 2010;49(3):2520-2525. doi:10.1016/j.neuroimage.2009.06.018
10. Sack I, Jöhrens K, Würfel J, Braun J. Structure-sensitive elastography: on the viscoelastic powerlaw behavior of in vivo human tissue in health and disease. *Soft Matter*. 2013;9(24):5672-5680. doi:10.1039/c3sm50552a
11. Hiscox L V, Johnson CL, Barnhill E, et al. Magnetic resonance elastography (MRE) of the human brain : technique , findings and clinical applications. *Phys Med Biol*. 2016;61:R401-R437. doi:10.1088/0031-9155/61/24/R401
12. Murphy MC, Huston J, Ehman RL. MR elastography of the brain and its application in neurological diseases. *Neuroimage*. 2019;187(August 2017):176-183. doi:10.1016/j.neuroimage.2017.10.008
13. McIlvain G, Tracy JB, Chaze CA, et al. Brain Stiffness Relates to Dynamic Balance Reactions in Children with Cerebral Palsy. *J Child Neurol*. 2020. doi:10.1177/0883073820909274
14. Noll DC, Meyer CH, Pauly JM, Nishimura DG, Macovski A. A homogeneity correction method for magnetic resonance imaging with time-varying gradients. *IEEE Trans Med Imaging*. 1991;10(4):629-637. doi:10.1109/42.108599
15. Jezzard P, Clare S. Sources of distortion in functional MRI data. *Hum Brain Mapp*. 1999;8(2-3):80-85. doi:10.1002/(SICI)1097-0193
16. Reichenbach J, Venkatesan R, Yablonskiy D, Thompson MR, Lai S, Haacke EM. Theory and Application of Static Field Inhomogeneity Effects in Gradient- Echo Imaging. *J Magn Reson Imaging*. 1997;7:266-279.
17. Sumanaweera T, Glover G, Song S, Adler J, Nape S. Quantifying MRI Geometric Distortion in Tissue. *Magn Reson Med*. 1994;31:40-47.
18. Mariappan YK, Glaser KJ, Richard L Ehman. Magnetic Resonance Elastography: A Review. *Clin Anat*. 2010;23(5):497-511. doi:10.1002/ca.21006
19. Johnson CL, Holtrop JL, McGarry MDJ, et al. 3D multislab, multishot acquisition for fast, whole-brain MR elastography with high signal-to-noise efficiency. *Magn Reson Med*. 2014;71(2):477-485. doi:10.1002/mrm.25065
20. Griswold MA, Jakob PM, Heidemann RM, et al. Acquisitions (GRAPPA). *Magn Reson Med*. 2002;47:1202-1210. doi:10.1002/mrm.10171
21. Pruessmann KP, Weiger M, Scheidegger MB, Boesiger P. SENSE: sensitivity encoding for fast MRI. *Magn Reson Med*. 1999;42(5):952-962. http://www.ncbi.nlm.nih.gov/pubmed/10542355.
22. Glover GH. Simple Analytic Spiral K-Space Algorithm. *Magn Reson Med*. 1999;415:412-415.
23. Johnson CL, McGarry MDJ, Van Houten EEW, et al. Magnetic resonance elastography of the brain using multishot spiral readouts with self-navigated motion correction. *Magn Reson Med*. 2013;70(2):404-412. doi:10.1002/mrm.24473
24. Campbell-Washburn AE, Xue H, Lederman RJ, Faranesh AZ, Hansen MS. Real-time distortion correction of spiral and echo planar images using the gradient system impulse response function. *Magn Reson Med*. 2016;75(6):2278-2285. doi:10.1002/mrm.25788
25. Glover GH. Spiral imaging in fMRI. *Neuroimage*. 2012;62(2):706-712. doi:10.1016/j.neuroimage.2011.10.039
26. Reber PJ, Wong EC, Buxton RB, Frank LR. Correction of Off Resonance-Related Distortion in Echo- Planar Imaging Using EPI-Based Field Maps. *Magn Reson Med*. 1998;39:328-330.
27. Holland D, Kuperman JM, Dale AM. Efficient correction of inhomogeneous static magnetic field-induced distortion in Echo Planar Imaging. *Neuroimage*. 2010;50(1):175-183. doi:10.1016/j.neuroimage.2009.11.044
28. Sutton BP, Noll DC, Fessler JA. Fast, Iterative Image Reconstruction for MRI in the Presence of Field Inhomogeneities. *IEEE Trans Med Imaging*. 2003;22(2):178-188.
29. Embleton K V, Haroon HA, Morris DM, Ralph MAL, Parker GJM. Distortion Correction for Diffusion-Weighted MRI Tractography and fMRI in the Temporal Lobes. *Hum Brain Mapp*. 2010;31:1570-1587.

doi:10.1002/hbm.20959
30. Bihan D Le, Poupon C, Amadon A. Artifacts and Pitfalls in Diffusion MRI. 2006;488:478-488. doi:10.1002/jmri.20683
31. Hutton C, Bork A, Josephs O, Deichmann R, Ashburner J, Turner R. Image Distortion Correction in fMRI : A Quantitative Evaluation. *Neuroimage*. 2002;16:217-240. doi:10.1006/nimg.2001.1054
32. Fehlner A, Hirsch S, Weygandt M, et al. Increasing the Spatial Resolution and Sensitivity of Magnetic Resonance Elastography by Correcting for Subject Motion and Susceptibility-Induced Image Distortions. *J Magn Reson Imaging*. 2017;46:134-141. doi:10.1002/jmri.25516
33. McGarry MDJ, Houten EEW Van, Johnson CL, et al. Multiresolution MR elastography using nonlinear inversion. *Med Phys*. 2012;39(6388):6388-6396. doi:10.1118/1.4754649
34. Okamoto RJ, Clayton EH, Bayly P V. Viscoelastic properties of soft gels: Comparison of magnetic resonance elastography and dynamic shear testing in the shear wave regime. *Phys Med Biol*. 2011;56(19):6379-6400. doi:10.1088/0031-9155/56/19/014
35. Manduca A, Oliphant TE, Dresner MA, et al. Magnetic resonance elastography: Non-invasive mapping of tissue elasticity. *Med Image Anal*. 2001;5(4):237-254. doi:10.1016/S1361-8415(00)00039-6
36. Johnson CL, McGarry MDJ, Gharibans AA, et al. Local mechanical properties of white matter structures in the human brain. *Neuroimage*. 2013;79:145-152. doi:10.1016/j.neuroimage.2013.04.089
37. McIlvain G, Clements RG, Magoon EM, Spielberg JM, Telzer EH, Johnson CL. Viscoelasticity of reward and control systems in adolescent risk taking. *Neuroimage*. 2020;215(February):116850. doi:10.1016/j.neuroimage.2020.116850
38. McGarry MDJJ, Van Houten EEW, Perrĩez PR, Pattison AJ, Weaver JB, Paulsen KD. An octahedral shear strain-based measure of SNR for 3D MR elastography. *Phys Med Biol*. 2011;56(13):153-164. doi:10.1088/0031-9155/56/13/N02
39. Delgorio PL, Hiscox L V, Daugherty AM, et al. Effect of Aging on the Viscoelastic Properties of Hippocampal Subfields Assessed with High-Resolution MR Elastography. *Cereb Cortex*. 2021:1-13. doi:10.1093/cercor/bhaa388
40. McGarry MDJ. Improvement and evaluation of nonlinear inversion MR Elastography. 2013.
41. Johnson CL, Schwarb H, D.J. McGarry M, et al. Viscoelasticity of subcortical gray matter structures. *Hum Brain Mapp*. 2016;37:4221-4233. doi:10.1002/hbm.23314
42. McGarry MDJ, Johnson CL, Sutton BP, et al. Suitability of poroelastic and viscoelastic mechanical models for high and low frequency MR elastography. *Med Phys*. 2015;42(2):947-957. doi:10.1118/1.4905048
43. McGarry M, Van Houten E, Guertler C, et al. A heterogenous, time harmonic, nearly incompressible transverse isotropic finite element brain simulation platform for MR elastography. *Phys Med Biol*. 2020.
44. Fessler JA, Sutton BP. Nonuniform fast Fourier transforms using min-max interpolation. *IEEE Trans Signal Process*. 2003;51(2):560-574. doi:10.1109/TSP.2002.807005
45. Ngo GC, Wong CN, Guo S, Paine T, Kramer AF, Sutton BP. Magnetic susceptibility-induced echo-time shifts: Is there a bias in age-related fMRI studies? *J Magn Reson Imaging*. 2017;45(1):207-214. doi:10.1002/jmri.25347
46. Jenkinson M, Beckmann CF, Behrens TEJJ, Woolrich MW, Smith SM. Fsl. *Neuroimage*. 2012;62(2):782-790. doi:10.1016/j.neuroimage.2011.09.015
47. McIlvain G, Ganji E, Cooper C, Killian ML, Ogunnaike BA, Johnson CL. Reliable preparation of agarose phantoms for use in quantitative magnetic resonance elastography. *J Mech Behav Biomed Mater*. 2019;97(April):65-73. doi:10.1016/j.jmbbm.2019.05.001
48. Pruessmann KP, Weiger M, Börnert P, Boesiger P. Advances in sensitivity encoding with arbitrary k-space trajectories. *Magn Reson Med*. 2001;46(4):638-651. doi:10.1002/mrm.1241
49. Jenkinson M, Bannister P, Brady M, Smith S. Improved optimization for the robust and accurate linear registration and motion correction of brain images. *Neuroimage*. 2002;17(2):825-841. doi:10.1016/S1053-8119(02)91132-8
50. Johnson CL, Holtrop JL, Anderson AT, Sutton BP. Brain MR Elastography with Multiband Excitation and Nonlinear Motion-Induced Phase Error Correction. In: *24th Annual Meeting of the Interational Society for Magnetic Resonance in Medicine, Singapore*. ; 2016:p 1951.
51. Cerjanic A, Holtrop JL, Ngo GC, et al. PowerGrid: A open source library for accelerated iterative magnetic resonance image reconstruction. *Proc Intl Soc Mag Reson Med*. 2016:14-17.
52. Desikan RS, Ségonne F, Fischl B, et al. An automated labeling system for subdividing the human cerebral cortex on MRI scans into gyral based regions of interest. *Neuroimage*. 2006;31(3):968-980.

doi:10.1016/j.neuroimage.2006.01.021

53. Andersson JLR, Smith SM, Jenkinson M. FNIRT - FMRIB; non-linear image registration tool. *Fourteenth Annu Meet Organ Hum Brain Mapping, Melbourne, Aust*. 2008:496.
54. Jezzard P, Balaban RS. Correction for Geometric Distortion in Echo-Planar Images from B0 Field Variations. *Magn Reson Med*. 1995;34(1):65-73. doi:10.1002/mrm.1910340111
55. Smith DR, Guertler CA, Okamoto RJ, Romano AJ, Bayly P V. Multi-Excitation Magnetic Resonance Elastography of the Brain : Wave Propagation in Anisotropic White Matter. *J Biomed Eng*. 2020;142(July). doi:10.1115/1.4046199
56. Okamoto RJ, Romano AJ, Johnson CL, Bayly P V. Insights Into Traumatic Brain Injury From MRI of Harmonic Brain Motion. *J Exp Neurosci*. 2019;13. doi:10.1177/1179069519840444
57. van Gorkum RJH, von Deuster C, Guenthner C, Stoeck CT, Kozerke S. Analysis and correction of off-resonance artifacts in echo-planar cardiac diffusion tensor imaging. *Magn Reson Med*. 2020;84(5):2561-2576. doi:10.1002/mrm.28318
58. Block KT, Frahm J. Spiral imaging: A critical appraisal. *J Magn Reson Imaging*. 2005;21(6):657-668. doi:10.1002/jmri.20320
59. Lam F, Sutton BP. Intravoxel B0 inhomogeneity corrected reconstruction using a low-rank encoding operator. *Magn Reson Med*. 2020;84(2):885-894. doi:10.1002/mrm.28182
60. Ngo GC, Bilgic B, Gagoski BA, Sutton BP. Correction of magnetic field inhomogeneity effects for fast quantitative susceptibility mapping. *Magn Reson Med*. 2019;81(3):1645-1658. doi:10.1002/mrm.27516
61. Chaze CA, McIlvain G, Smith DR, et al. Altered brain tissue stiffness in pediatric cerebral palsy measured by magnetic resonance elastography. *NeuroImage Clin*. 2019;22. doi:10.1016/j.nicl.2019.101750
62. Schwarb H, Johnson CL, McGarry MDJ, Cohen NJ. Medial temporal lobe viscoelasticity and relational memory performance. *Neuroimage*. 2016;132:534-541. doi:10.1016/j.neuroimage.2016.02.059
63. Hiscox L, Johnson CL, McGarry MDJ, et al. Hippocampal viscoelasticity and episodic memory performance in healthy older adults examined with magnetic resonance elastography. *Brain Imaging Behav*. 2018. doi:10.1007/s11682-018-9988-8
64. Johnson CL, Schwarb H, Horecka KM, et al. Double dissociation of structure-function relationships in memory and fluid intelligence observed with magnetic resonance elastography. *Neuroimage*. 2018;171(December 2017):99-106. doi:10.1016/j.neuroimage.2018.01.007
65. Irfanoglu MO, Sarlls J, Nayak A, Pierpaoli C. Evaluating corrections for Eddy-currents and other EPI distortions in diffusion MRI: methodology and a dataset for benchmarking. *Magn Reson Med*. 2019;81(4):2774-2787. doi:10.1002/mrm.27577
66. Tao S, Trzasko JD, Gunter JL, et al. Gradient nonlinearity calibration and correction for a compact, asymmetric magnetic resonance imaging gradient system. *Physiol Behav*. 2018;62(2):18-31. doi:10.1088/1361-6560/aa524f